

# Disentangling Interacting Systems with Fermionic Gaussian Circuits: Application to the Single Impurity Anderson Model

Ang-Kun Wu,<sup>1,2</sup> Matthew T. Fishman,<sup>2</sup> J. H. Pixley,<sup>1,2</sup> and E. M. Stoudenmire<sup>2</sup>

<sup>1</sup>*Department of Physics and Astronomy, Center for Materials Theory,  
Rutgers University, Piscataway, New Jersey 08854, USA*

<sup>2</sup>*Center for Computational Quantum Physics, Flatiron Institute, New York, New York 10010, USA*  
(Dated: December 21, 2022)

Tensor network representations of quantum many-body states provide powerful tools for strongly correlated systems, tailored to capture local correlations such as ground states exhibiting entanglement area laws. When applying tensor network states to interacting fermionic systems, a proper choice of basis or orbitals can greatly reduce the bond dimension of tensors and speed up calculations. We introduce such a change of basis with unitary gates obtained via compressing fermionic Gaussian states into quantum circuits corresponding to various tensor networks. These circuits can reduce the ground state entanglement entropy and improve the performance of algorithms such as the density matrix renormalization group. We study the 1D single impurity Anderson model to show the power of the method in improving computational efficiency and interpreting impurity physics. Furthermore, fermionic Gaussian circuits also show potential for suppressing entanglement during the time evolution of a low-lying excited state that is used to compute the impurity Green's function. Lastly, we consider Gaussian multi-scale entanglement renormalization ansatz (GMERA) circuits which compress fermionic Gaussian states hierarchically. The emergent coarse-grained physical models from these GMERA circuits are studied in terms of their entanglement properties and suitability for performing time evolution.

## I. INTRODUCTION

Tensor network methods, originating from the density matrix renormalization group (DMRG), provide a powerful set of tools for studying many-body quantum systems [1–5]. The organizing principle of these methods is entanglement. States with low entanglement can be approximately factored into a contracted network of small tensors, leading to fast and precise algorithms. The size of the indices connecting the tensors, known as the bond dimension, is tied to the amount of entanglement and directly controls the cost of tensor network calculations.

Entanglement is exquisitely sensitive to the basis in which a state is represented. Non-interacting fermion systems exhibit some of the most highly entangled ground states [6–12] yet become completely unentangled when transformed into the momentum basis (assuming periodic boundary conditions). More generally, low-energy states of local Hamiltonians typically obey the *area law* (up to logarithmic corrections), meaning the entanglement of subsystem of volume  $l^d$  in dimension  $d$  scales as its area  $\sim l^{d-1}$ . Though the area law explains why a wide class of low-energy states have limited entanglement in real space, it does not imply that real space is the basis with the *lowest* entanglement.

The insight that another basis besides real space could yield more efficient tensor network calculations has been put into practice for some time, a notable example being the work by Krumnow, Eisert, and Legeza on computing basis transformations [13–15]. Their approach optimizes local two-site unitary gates so as to minimize the entanglement across a given bipartition of the system, often resulting in significantly lower entanglement throughout the system. It has been successfully applied to ground

states of interacting one- and two-dimensional systems and to dynamical systems.

In a separate advance, Fishman and White [16] showed how the problem of transforming Gaussian fermionic states into tensor networks could be solved by finding quantum circuits—fermionic Gaussian circuits—which provide a basis where the Gaussian state becomes unentangled. Their approach has many appealing aspects, such as a fast, direct method for computing circuits that preserve the locality of the Hamiltonian. These many-body circuits are equivalent to canonical transformations of the single-particle basis and map straightforwardly into known classes of tensor networks, like matrix product states (MPS) [1, 2, 17], tree tensor networks (TTN) [18], and multi-scale entanglement renormalization ansatz (MERA) networks [19–21].

The relevance of such Gaussian circuits for interacting, non-Gaussian systems has been unclear. In this work, we synthesize the above ideas, utilizing basis transformations obtained from non-interacting systems to reduce the entanglement of interacting systems. We find that Gaussian circuit transformations can significantly speed up tensor network calculations and yield physical insights. To demonstrate our approach, we consider the single impurity Anderson model in one dimension [22], whose physical properties and entanglement structure are known and provide a rich testbed for our methods.

After demonstrating that Gaussian circuits can uncover a basis in which the ground state has low entanglement, we show how certain physical properties also become more transparent in the new basis. The same approach can also reduce the entanglement of a system undergoing quench dynamics.

Beyond simpler Gaussian circuit transformations

based on matrix product states, we also consider multi-scale circuits known as Gaussian MERA (GMERA). In addition to reducing entanglement, GMERA circuits provide a physical interpretation of the transformed degrees of freedom. The basis introduced by a conventional GMERA is analogous to a “star geometry” bath used in impurity solvers [23, 24] while a modified boundary GMERA [25–27] is analogous to a Wilson “chain geometry” bath [28, 29]. The GMERA approach lets us identify an important subset of sites in the transformed basis, and we show that reducing the bath to consist of these sites only is sufficient for obtaining dynamical properties.

We begin by reviewing the technology of fermionic Gaussian circuits in Sec. II. After introducing the impurity models in Sec. III, we explore how Gaussian MPS (GMPS) circuits can drastically reduce their entanglement in Sec. IV, resulting in much faster DMRG solutions without ever passing through a more highly entangled basis. In Sec. V we show how the Gaussian circuit transformations reveal Kondo screening physics and in Sec. VI we demonstrate that the disentangling can succeed in systems undergoing dynamics, too. Finally, Sec. VII explores two types of GMERA circuits, the physical interpretation of the non-interacting bath following each GMERA transformation, and the possibility of simulating the impurity model in a smaller coarse-grained space.

## II. REVIEW: FERMIONIC GAUSSIAN TENSOR NETWORK CIRCUITS

Before turning to interacting systems, we briefly review the technology of compressing fermionic Gaussian states, following Ref. [16], through which *fermionic Gaussian circuits* [16, 30] (also known as *matchgate circuits* [31, 32]) are defined. Different layouts and patterns of these circuits produce various Gaussian tensor networks, such as the GMPS and the GMERA circuits.

Given a non-interacting system with a Hamiltonian

$$H_0 = \sum_{ij} h_{ij} c_i^\dagger c_j, \quad (1)$$

and  $c_i^\dagger$  the spinless fermionic creation operator at site  $i$ , one can straightforwardly construct its ground state by diagonalizing the matrix  $h = UDU^\dagger$  and filling the orbitals (columns of  $U$ ) having the lowest energies (eigenvalues of  $h$ ). The ground state can be written as

$$|\psi_0\rangle = \prod_{k=1}^{N_F} c_k^\dagger |\Omega\rangle \quad (2)$$

where  $N_F$  is the number of fermions and  $|\Omega\rangle$  is the vacuum.

The construction of fermionic Gaussian circuits is

based on the correlation matrix

$$\Lambda_{ij} = \langle \psi_0 | c_i^\dagger c_j | \psi_0 \rangle = \sum_{k=1}^{N_F} U_{ik}^* U_{jk}, \quad (3)$$

where the goal is to approximately diagonalize  $\Lambda$  with a circuit that also preserves locality. In a basis where  $\Lambda$  is diagonal, the state will have zero entanglement [16, 33].

An important fact about the correlation matrix is that, for a pure and number conserving fermionic state, its eigenvalues are all exactly 0 or 1, corresponding to empty or filled orbitals. For 1D states obeying the entanglement area law, such as ground states of gapped and local Hamiltonians, there exists a contiguous subblock  $\mathcal{B}$  of size  $B$  that is independent of system size  $N$  in which one of the eigenvalues will be close to 0 or 1. For ground states of gapless 1D systems, the block size needed to find an eigenvalue close to 0 or 1 only grows modestly with system size as  $\log N$  [16].

Here we give a brief summary of the deterministic algorithm for diagonalizing a correlation matrix with local rotations. Local rotations of the form:

$$R(\theta) = \begin{pmatrix} \cos \theta & -\sin \theta \\ \sin \theta & \cos \theta \end{pmatrix} \quad (4)$$

are used to transform  $2 \times 2$  blocks of  $\mathcal{B}$ , much like in the  $QR$  factorization of a matrix based on Givens rotations. The rotations  $R(\theta)$  are chosen to isolate an *inactive orbital* or eigenvector of  $\mathcal{B}$  with eigenvalue close to 0 or 1 in the upper-left corner of the block  $\mathcal{B}$  of  $\Lambda$ . The rotation angle  $\theta$  is determined numerically from an eigenvector, for example if the eigenvector is  $v = (v_1, v_2)^T$ , the angle  $\theta = -\arctan \frac{v_2}{v_1}$  rotates the vector to  $v' = (1, 0)^T$ . Higher dimensional eigenvectors can be rotated iteratively [16]. In the resulting basis, the first site of the transformed block will correspond to the inactive orbital which will be approximately disentangled from the rest of the system.

For each subblock  $\mathcal{B}$ , one can obtain a minimal set of local  $B - 1$  rotation gates which act together as  $R_{\mathcal{B}}$  that isolate an inactive orbital of  $\mathcal{B}$  through  $B - 1$  rotations. After discarding the row and column corresponding to the disentangled (inactive) site, one can repeat the process on a new block, expanding the block as needed to find the next inactive orbital by including adjacent rows and columns of the correlation matrix. Once all blocks have had their most inactive orbital disentangled, the entire correlation matrix will be approximately diagonalized by a sequence of gates

$$R \equiv R_{\mathcal{B}_1} R_{\mathcal{B}_2} \cdots R_{\mathcal{B}_{N-1}}, \quad (5)$$

as described in detail in [16, 30]. At the single-particle level, the matrix  $R$  defines a transformation of the  $c_i$  operators into new operators

$$f_r = \sum_i R_{ri} c_i, \quad (6)$$

which annihilate fermions in the transformed basis indexed by  $r$ . These orbitals generally differ from the single-particle eigenstates, in that they are local and do not diagonalize the quadratic Hamiltonian.

Once the set of single-particle transformations  $R$  have been found, these transformations can be “lifted” or promoted into many-body quantum gates forming a quantum circuit. We show an example of an (inverse) GMPS circuit acting on a many-body MPS in Fig. 1. Specifically, an individual matrix  $R(\theta)$  acting on the  $(j, j + 1)$  block of the correlation matrix can be reinterpreted as a unitary gate  $\hat{R}_{j,j+1}(\theta)$  acting on sites  $j, j + 1$  and having the following form

$$\hat{R}(\theta) = \begin{pmatrix} 1 & 0 & 0 & 0 \\ 0 & \cos \theta & -\sin \theta & 0 \\ 0 & \sin \theta & \cos \theta & 0 \\ 0 & 0 & 0 & 1 \end{pmatrix} \quad (7)$$

The 4 by 4 matrix above acts in the basis  $\{|\Omega\rangle, c_j^\dagger|\Omega\rangle, c_{j+1}^\dagger|\Omega\rangle, c_j^\dagger c_{j+1}^\dagger|\Omega\rangle\}$  of the  $j$  and  $j + 1$  sites. These  $\hat{R}_{j,j+1}(\theta)$  are the blue tensors shown in the circuit at the top of Fig. 1. The red ellipse in the figure highlights the tensors acting within the first block  $\mathcal{B}_1 = \{1, 2, 3, 4\}$ , assuming a block size of  $B = 4$ .

Fermionic Gaussian circuits obtained as described above are called Gaussian matrix product state (GMPS) circuits. A slight modification of the procedure leads to Gaussian MERA (GMERA) circuits discussed in Sec. VII. Once the circuits are obtained, they can be used to efficiently transform and disentangle many-body states in the MPS representation as shown in Fig. 1.

The techniques above can be straightforwardly extended to apply to fermions with spin or to systems not preserving fermion number [34], though we will continue to use the spinless fermion formalism for reasons explained in the next section.

### III. IMPURITY MODEL SYSTEM

To explore the ability of Gaussian circuits to disentangle interacting systems, we will study the 1D single impurity Anderson model (SIAM) [22]. This is an ideal test system since the interaction is local and act only on the impurity site. The properties of this model are well understood, allowing us to physically interpret properties revealed by the transformations.

The Hamiltonian for the SIAM is

$$H_A = H_{\text{imp}} + H_{\text{hyb}} + H_{\text{bath}}. \quad (8)$$

with the impurity terms

$$H_{\text{imp}} = \epsilon_d(\hat{n}_{d\uparrow} + \hat{n}_{d\downarrow}) + U\hat{n}_{d\uparrow}\hat{n}_{d\downarrow}, \quad (9)$$

describing a degenerate impurity orbital occupied by  $\hat{n}_{d\sigma} = d_\sigma^\dagger d_\sigma$  electrons having spin  $\sigma$ , energy  $\epsilon_d$ , and an on-site Coulomb repulsion  $U$ . The second term hybridizes

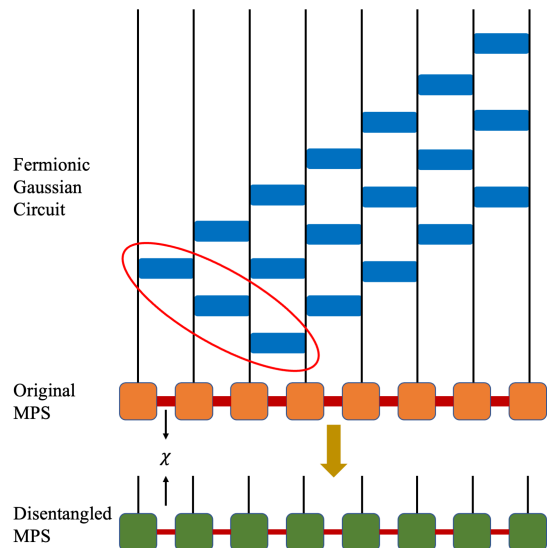


FIG. 1. Demonstration of a fermionic Gaussian circuit computed from a fermionic Gaussian state being applied to an MPS. The MPS ground state in the original basis is composed of smaller tensors (orange squares) with physical dimensions (black lines) and connected by bonds (red edges). After applying the conjugated and reversed fermionic Gaussian gates  $\hat{R}(\theta_i)^\dagger$  (blue rectangles) with fixed block size  $B = 4$ , the MPS is transformed into a new basis (green squares), hopefully with a smaller bond dimensions  $\chi$ . The  $B - 1$  gates acting on a single block of size  $B = 4$ , denoted in the text by  $\hat{R}_B$ , are marked by the red ellipse. In the case when the original MPS is a fermionic Gaussian state and the fermionic Gaussian circuit is constructed from its correlation matrix, the disentangled state will have a bond dimension of  $\chi = 1$ , approximately disentangled up to controllable errors in the circuit construction.

the impurity with the first bath electron (denoted as site 2)

$$H_{\text{hyb}} = -V \sum_{\sigma} (d_{\sigma}^{\dagger} c_{2\sigma} + \text{H.c.}), \quad (10)$$

where  $V$  is the hybridization strength. The bath electrons are taken to be the 1D tight-binding model

$$H_{\text{bath}} = -t \sum_{r=2,\sigma}^{N-1} (c_{r\sigma}^{\dagger} c_{(r+1)\sigma} + \text{H.c.}), \quad (11)$$

with hopping strength  $t$  and total number of sites  $N$ , including the impurity. For all cases, we keep the particle-hole symmetry for the impurity  $U = -2\epsilon_d$ .

Computationally, when using the spinful  $S = 1/2$  local Hilbert space  $|0\rangle, |\uparrow\rangle, |\downarrow\rangle, |\uparrow\downarrow\rangle$  for each site in the original geometry of the model, the DMRG algorithm requires high bond dimensions  $\chi$  (thousands for system sizes of hundreds) to obtain good precision. Without changing the physics, one can rewrite the model by separating the spin up and down operators

$$a_{-j} \equiv c_{j\uparrow}, \quad a_j \equiv c_{j\downarrow}, \quad (12)$$

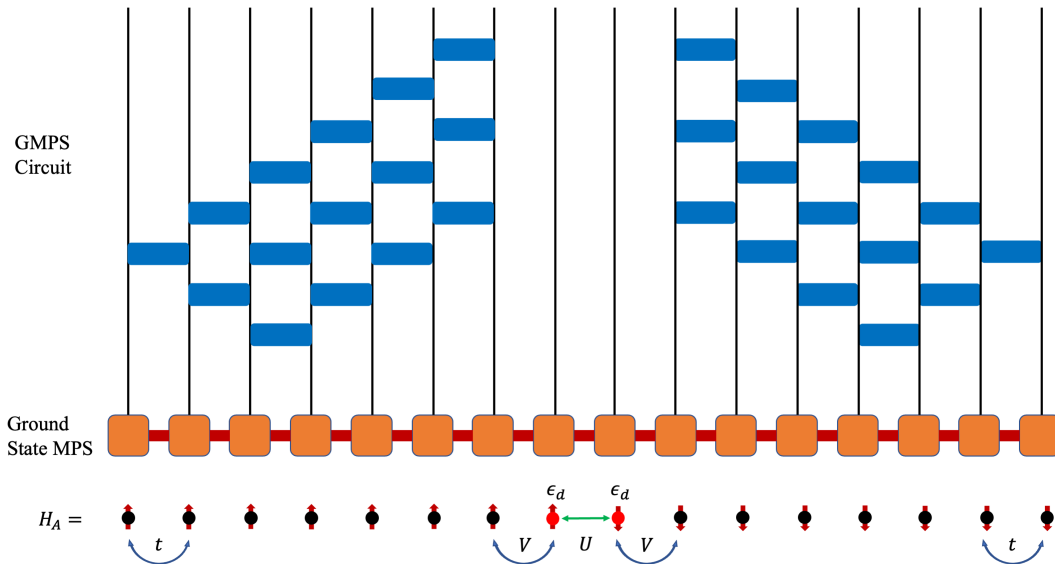


FIG. 2. Demonstration of the split-site geometry of the impurity model and the corresponding GMPS circuit. In the bottom, the split-site geometry of the impurity model  $H_A$  with  $N = 8$  is shown with all up spin degrees freedom in the left-hand side while all down spins in the right with Eq. 12. The corresponding GMPS circuit with block size  $B = 4$  can be obtained by symmetrizing the circuit from the up spin part (non-interacting limit). To maintain the locality of the interaction  $U$ , rotation gates at the impurity sites are avoided. Blocks of the circuit start from the two ends of the chain, each of which consist of  $B - 1$  unitary gates (blue rectangles).

where  $j = 1, 2, \dots, N$  and  $j = 1$  denotes the impurity operator  $a_{-1} \equiv d_{\uparrow}, a_1 \equiv d_{\downarrow}$ . Such a *split-site representation* leads to more favorable entanglement and MPS bond dimensions. This “unfolded” representation has been used often for studying impurity systems with MPS techniques [35–38]. The geometry of this split-site representation and the corresponding GMPS circuit are shown in Fig. 2. The detailed model in terms of operators  $a_j$  can be found in Appendix A.

Throughout, we will be especially interested in studying the von Neumann entanglement entropy, defined as

$$S = -\text{Tr} \rho_A \ln \rho_A \quad (13)$$

where  $\rho_A = \text{Tr}_B [|\Psi\rangle\langle\Psi|]$  is the reduced density matrix of system  $A$  and  $|\Psi\rangle$  is the quantum many-body state of interest.

The MPS formalism allows one to obtain the entropy  $S$  efficiently when  $A$  is either a contiguous region of sites of the form  $1, 2, \dots, L_A$  or when  $A$  is a small region of neighboring sites. Computing the entanglement entropy of what would be a simple bipartitioning of the sites in real space (before splitting up and down spin degrees of freedom) involves a more complicated ABA partitioning in the split-site representation. We describe how to compute the entanglement entropy with MPS in the split-site representation in Appendix B.

#### IV. DISENTANGLING IMPURITY MODELS WITH GAUSSIAN MPS CIRCUITS

We now explore the power of Gaussian MPS circuits for disentangling ground states. After disentangling an interacting ground state MPS to demonstrate the idea, we use the circuit to change the basis of the Hamiltonian *before* computing the ground state to accelerate tensor network calculations.

##### A. Disentangling the ground state

Using DMRG, we obtain the ground state of the single-impurity Anderson model (SIAM) as an MPS. To disentangle this ground state MPS, we compute a GMPS circuit from the  $U = 0$  limit of the SIAM, apply this circuit to the ground state MPS, and study its entanglement in the transformed basis.

Figure 2 shows this process in more detail, for the split-site geometry we used. The GMPS transformation starts from the ends of the finite leads and proceeds toward the impurity. Any gates touching the impurity are omitted. Because of the left-right (up and down spin) symmetry of the model we use the same gates from both ends.

Figure 3(a) shows the entanglement entropy before and after the transformation for both  $U/t = 1$  and  $U/t = 10$ , showing only the down-spin (right-hand) side of the system. The entanglement starts out rather high in the orig-

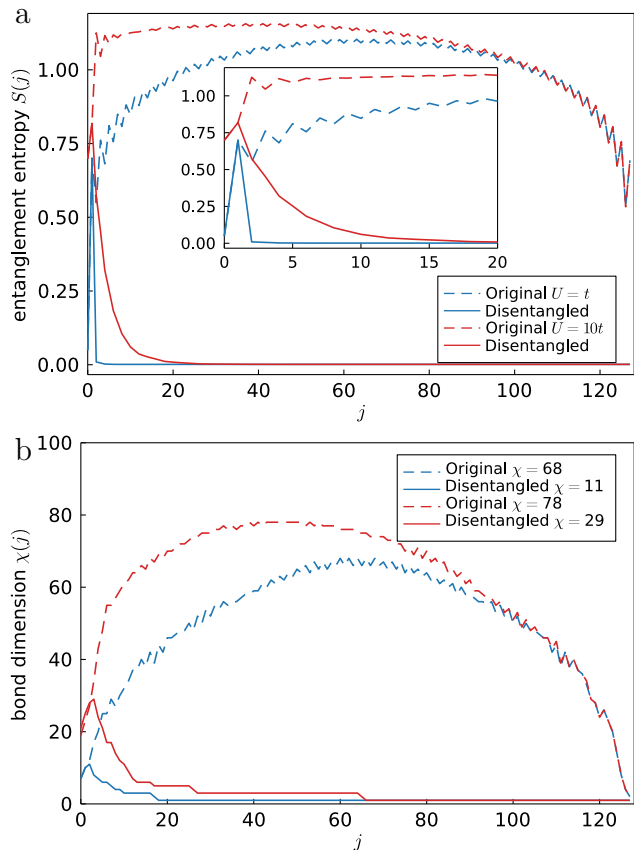


FIG. 3. Entanglement entropy and MPS bond dimension before and after the fermionic Gaussian circuit transformation. Properties in the original basis (dashed curves) are compared with the same properties in the transformed basis (solid curves) when using the GMPS circuit for systems  $N = 128, V = t$ . Systems with small interaction  $U/t = 1$  are shown in blue and strong interaction  $U/t = 10$  in red. The upper panel (a) shows the entanglement entropy  $S$  as a function of bipartite (down spins) site distance  $j$  away from the impurity site. Inset: entanglement entropy close to the impurity. The lower panel (b) shows MPS bond dimensions  $\chi(j)$  at each bond. The legend shows the maximum MPS bond dimension  $\chi$  (when using a fixed truncation error cutoff in DMRG of  $10^{-8}$ ).

inal basis, with an “arc” shape characteristic of gapless systems. After the GMPS transformation, the entanglement is reduced nearly to zero over most of the system except for a region near the impurity. Remarkably, the same circuit based on the  $U = 0$  limit works well in both cases. The MPS bond dimension  $\chi$  is also significantly reduced by the GMPS transformation (Fig. 3(b)).

Certain physical properties become apparent after the transformation, a phenomenon we study in more detail in Section V below. In the SIAM, the impurity is known to be screened by the bath electrons over a length scale  $\xi_K$ , the Kondo screening length, and should be primarily entangled with sites within this distance. The Kondo screening length is known to become larger as  $U/t$  in-

creases. Correspondingly, one can see in Fig. 3 that the region of finite entanglement near the impurity is in fact larger in the  $U/t = 10$  system than in the  $U/t = 1$  system.

## B. Transforming the Hamiltonian

The speed of a DMRG calculation depends on the entanglement of the state being calculated. But the approach of the previous section would not yield faster ground state calculations since the state was computed before the transformation was ever used. In this section, we exploit the dual nature of fermionic Gaussian circuits as both many-body quantum circuits and single-particle basis transformations [16] to transform the Hamiltonian before starting any DMRG calculations. It is not obvious this will work, as the more complicated form of the transformed Hamiltonian could offset gains from the less entangled state. But the tradeoff turns out to be very favorable.

To transform the Hamiltonian, we interpret the GMPS circuit as a “matrix circuit” of sparse Givens rotation matrices (Eq. 4) multiplied together to form a unitary single-particle transformation  $R$ . Using the definition  $f_r = \sum_j R_{rj} c_j$  of the fermion operators in the transformed basis, the quadratic part of the Hamiltonian transforms as

$$\begin{aligned} \sum_{jj'} t_{jj'} c_j^\dagger c_{j'} &= \sum_{rr'} \left( \sum_{jj'} R_{rj} t_{jj'} R_{r'j'}^* \right) f_r^\dagger f_{r'} \\ &= \sum_{rr'} \tilde{t}_{rr'} f_r^\dagger f_{r'} \end{aligned} \quad (14)$$

As in the previous section, any matrices (or “matrix gates”) in  $R$  that act on the impurity are dropped from the circuit. This choice keeps the impurity part of the Hamiltonian  $H_{\text{imp}}$  precisely the same after the change of basis and keeps the interaction  $U$  term local.

Running DMRG on the transformed Hamiltonian turns out to be much faster since the ground state has very low entanglement—see Fig. 4 for timings. The median sweep time is between 2.5 and 12.5 times *faster* than in the original basis, with greater speedups for the larger the system size.

Because the Hamiltonian is less local in the transformed basis, the bond dimension of its matrix product operator (MPO) representation will necessarily become larger than in the original basis. To compute the Hamiltonian MPO in the transformed basis, we use a compression algorithm based on Ref. 39 that is publicly available through the ITensor software [40]. The transformed MPO bond dimension grows logarithmically with system size (lower inset of Fig. 4), reaching  $\chi = 26$  for the largest system size of  $N = 512$ . This is in contrast to a bond dimension of  $\chi = 4$  in the original basis. An MPO bond dimension of  $\chi = 26$  is not very large in practice, and DMRG calculations scale only quadratically with the

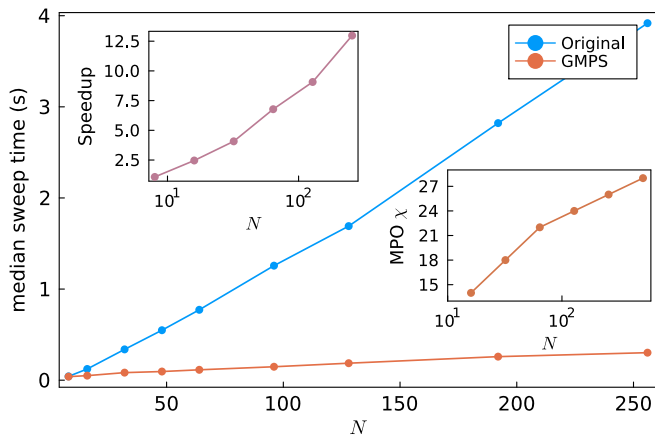


FIG. 4. Median DMRG sweep time in the original versus GMPS transformed basis as a function of system size  $N$ . Each DMRG calculation involved 20 sweeps and a truncation cut-off of  $10^{-6}$ ; the system used was  $U = t, V = t, \epsilon_d = -U/2$ . Top left inset: the speedup, defined as original sweep time divided by sweep time in the transformed basis, as a function of system size. Bottom right inset: the maximum bond dimensions  $\chi$  of MPO as a function of system sizes  $N$ , which asymptotically scale as  $\log(N)$ .

MPO bond dimension, versus as the cube of the MPS bond dimension, explaining why the “disentangled” calculations in the transformed basis can be so much faster despite a more complicated Hamiltonian.

We conclude this section by mentioning an interesting negative result. We attempted to reduce the MPO bond dimension further by discarding any quadratic Hamiltonian terms with an absolute value below a small threshold  $\tilde{t}_{ij} < \epsilon$ . But this led to *larger* MPO bond dimensions compared to keeping all quadratic terms—see Appendix D for details. In hindsight, this effect is probably due to the transformed  $\tilde{t}_{ij}$  decaying smoothly, whereas truncating them would introduce an artificially sharp step. Therefore a recommended practice is to keep all Hamiltonian terms in the transformed basis when compressing the Hamiltonian into an MPO.

## V. KONDO SCREENING PHYSICS IN THE TRANSFORMED BASIS

Gaussian circuit transformations remove entanglement by localizing “inactive” single-particle states. What physical properties become more transparent or easier to obtain in the transformed basis? We will demonstrate that universal Kondo physics emerges from entanglement in the transformed basis and show that this basis is practically useful for computing other physical properties to high accuracy.

Kondo physics emerges from the SIAM in the low-energy limit, where impurity occupancy becomes pinned to  $n_d = 1$  and a Schrieffer-Wolff transformation maps the

SIAM to an effective Kondo model in which the impurity couples to the bath only through a spin interaction (in the limit of particle hole symmetry). The strength of this spin interaction is called the Kondo (exchange) coupling and is given by

$$J_K = 8V^2D/U \quad (15)$$

with  $D$  the half bandwidth for the particle-hole symmetric case. A renormalization group (RG) analysis of the Kondo model (in the metallic and thermodynamic limit) shows the system always flows toward a strong-coupling fixed point where the impurity is screened by the bath electrons. The universal nature of the strong coupling Kondo screened fixed point implies that correlation functions, as well as the entanglement entropy, are scaling functions in terms of the Kondo screening length  $\xi_K$  given by

$$\xi_K \sim \frac{1}{\sqrt{UV^2}} \exp\left(\frac{\pi U}{8V^2}\right). \quad (16)$$

up to third order in  $J_K$  within the RG [41–43]. In real space, this length scale can be associated with the size of the Kondo screening cloud.

### A. Kondo Screening Length From Entanglement

A direct measure of the Kondo screening cloud is to study the behavior of the entanglement entropy at a distance  $r$  away from the impurity [42, 44–47]. It has been shown that the impurity entanglement entropy exhibits universal scaling behavior in terms of  $r/\xi_K$ . The impurity entanglement entropy in real space is defined as

$$S_{\text{imp}}(r, U) = S(r, U) - S^{(0)}(r), \quad (17)$$

$$S(r, U) = -\text{Tr}[\rho_r \ln \rho_r],$$

where  $S^{(0)}(r)$  is entanglement entropy only from the bath ( $U = 0, V = 0$ ), which can be obtained from the correlation matrix (Appendix A of [16]), and  $\rho_r$  is the reduced density matrix for the subsystem of the first  $r$  sites around the impurity, computed from the interacting state at finite  $U$ . Computing the entanglement entropy in the split-site representation is explained in more detail in the Appendix B. The impurity entanglement entropy oscillates between even and odd sites [42, 44, 48], so in what follows we will always average over even and odd sites numerically. There exists a scaling function such that

$$S_{\text{imp}}(r, U) = g\left(\frac{r}{\xi_K(U)}\right), \quad (18)$$

where  $g(x)$  is a universal scaling function.

The goal of the bath subtraction in Eq. (17) above is to reveal the location of the screening cloud, where deep inside the screening cloud  $r \ll \xi_K(U)$ ,  $S_{\text{imp}} = \ln 2$ , and outside of it  $r \gg \xi_K(U)$ ,  $S_{\text{imp}} \rightarrow 0$ . In the GMPS

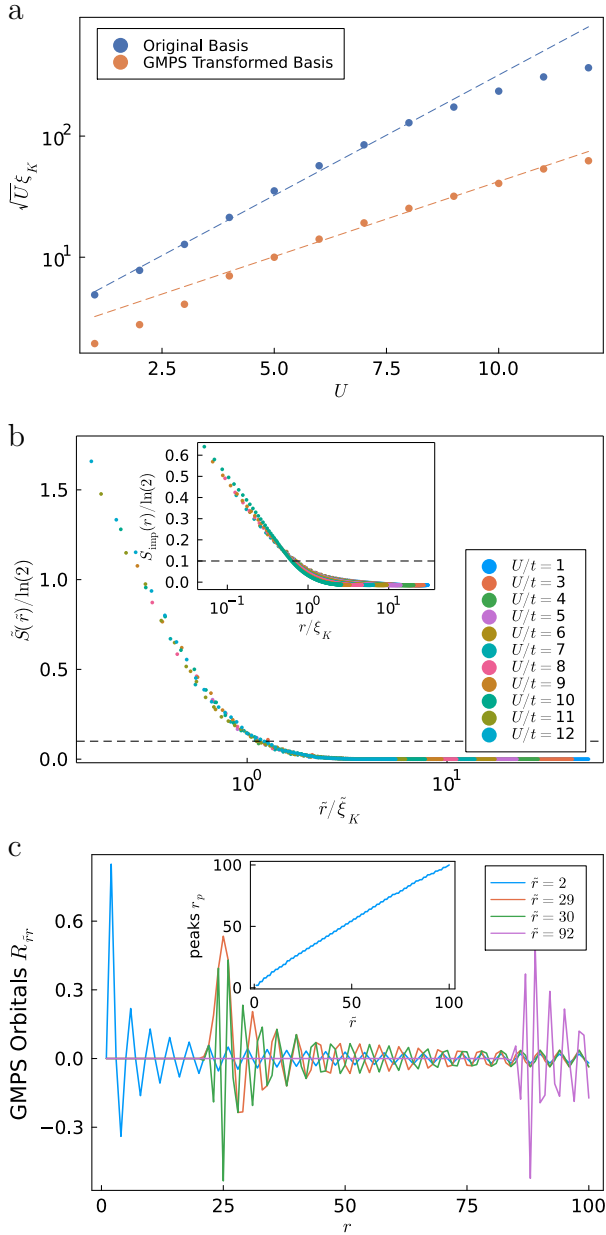


FIG. 5. Impurity entanglement entropy and Kondo screening length from systems  $N = 400$ ,  $V = t$ ,  $\epsilon_d = -U/2$  with various  $U \in [1, 12]$ . (a)  $\xi_K$ , defined as the length where the entanglement entropy drops below the threshold  $S_{\text{imp}}(\xi_K) = 0.1$ . (b) The collapse of entanglement entropy in the mapped GMPS basis,  $\tilde{S}(\tilde{r})$ , as a function of scaled distance  $\tilde{r}/\xi_K$  away from the impurity site, where  $\xi_K$  are obtained from (a). Inset: corresponding results for impurity entanglement entropy  $S_{\text{imp}}(r)$  (with subtraction of bath electron contribution) in the original basis. Note that in the original basis, we take middle locations across the even-odd result average. (c) Orbitals from the GMPS transformed basis with  $N = 100$ ,  $V = t$ .  $r$  denotes the distance from the impurity  $r = 1$  in real space. Inset: the peaks location  $r_p$  in real space versus orbital index  $\tilde{r}$  in the GMPS transformed basis.

transformed basis, the decay of the entanglement away from the impurity is naturally achieved and a subtraction of the non-interacting bath entanglement is no longer needed (see Fig. 3). However, it is not obvious that the entanglement in the transformed basis will exhibit universal scaling behavior similar to Eq. 18 since the distance  $\tilde{r}$  from the impurity in the transformed basis is not the same as the real-space distance  $r$ .

Nevertheless, Fig. 5 shows we can obtain universal information about the Kondo screening physics directly from the entanglement in the transformed basis. For the results in panel (a),  $\xi_K$  is determined in the GMPS transformed basis by finding the value of  $\tilde{r}$  such that  $S(\tilde{r} = \xi_K) = 0.1$ , where 0.1 is an arbitrary small threshold. We also perform an identical procedure in the original real space basis but using the quantity  $S_{\text{imp}}$  Eq. (17). The values of  $\xi_K$  determined this way scale with  $U$  as  $\sqrt{U}\xi_K \sim \exp(CU)$  over a wide range of  $U$  with some constant  $C$  (different for each basis) which fits qualitatively well with the expression in Eq. (16).

In panel (b), we scale the  $x$  axis by the Kondo length  $\xi_K$  and plot the transformed-basis entanglement against this rescaled axis. There is a clear scaling collapse for a range of  $U$ , even better than for the real-space  $S_{\text{imp}}$  results shown in the inset of Fig. 5(b), and without the difficulty of subtraction and even-odd averaging necessary to analyze the entanglement collapse in real space [44]. To understand better what the  $\tilde{r}$  distance means in the transformed basis, Fig. 5(c) also shows the orbitals  $R_{\tilde{r}r}$  in real space  $r$  corresponding to a specific site  $\tilde{r}$  in the transformed basis.

## B. Universal Collapse of Spin Correlators

Universal aspects of Kondo physics can also be realized through the correlations between the impurity spin and the non-interacting bath, given by

$$C(r) = \langle \mathbf{S}_d \cdot \mathbf{S}(r) \rangle = \langle \Psi_0 | \mathbf{S}_d \cdot \mathbf{S}(r) | \Psi_0 \rangle, \quad (19)$$

where  $\mathbf{S}_d = d_{\alpha}^{\dagger}(\boldsymbol{\sigma}_{\alpha\beta}/2)d_{\beta}$  and  $\mathbf{S}(r) = \frac{1}{2} \sum_{ss'} c_{r\alpha}^{\dagger} \boldsymbol{\sigma}_{\alpha\beta} c_{r\beta}$  is the impurity and conduction electron spin density, respectively, and  $\boldsymbol{\sigma}$  denotes a vector of Pauli matrices. The spin correlations exhibit a universal scaling collapse of the form [49–51]

$$C(r, U) = \frac{1}{\xi_K} f\left(\frac{r}{\xi_K}\right), \quad (20)$$

where  $f(x)$  is a universal scaling function.

In Fig. 6(a) we show the spin correlation function  $C(r, U = 10t)$  computed in real-space for various DMRG truncation error cutoffs (smaller cutoff means higher accuracy) or in the transformed basis using a moderate cutoff. We show results for even sites only, to avoid oscillations. To obtain the transformed-basis results, we first converge the DMRG calculation, apply the GMPS circuit

to map back to the original basis, then compute measurements. From the figure we can see that the transformed-basis approach produces results matching the highest-accuracy calculation in the original basis with a much more moderate computational effort (smaller bond dimension).

The advantage of performing computations using the transformed basis becomes even more noticeable when we consider a range of interactions  $U$  in Fig. 6(b) and plot the spin correlations with the axes rescaled by  $\xi_K$  so as to obtain a universal scaling collapse, using a value of  $\xi_K$  determined analytically from Eq. 16. The main figure shows the excellent collapse obtained for  $1 \leq U/t \leq 12$  when using a DMRG cutoff of  $10^{-6}$  and the transformed-basis approach. The inset shows a similar calculation but performed entirely in the original basis, exhibiting noticeable deviations from the universal form at larger values of  $r$ .

## VI. TIME EVOLVED STATES TRANSFORMED BY FERMIONIC GAUSSIAN CIRCUITS

An interesting question is whether we can use the GMPS circuit we computed from the non-interacting ground state to help reduce the entanglement of systems undergoing dynamics.

To understand the dynamics of the impurity, we consider time evolution of state with a local quench at the impurity site at time  $t = 0$

$$|\Phi(t)\rangle \equiv U(t)|\Phi(0)\rangle, \quad |\Phi(0)\rangle \equiv d_\downarrow |\Psi_0\rangle \quad (21)$$

where  $|\Psi_0\rangle$  is the many-body ground state and  $U(t)$  is the time-evolution operator. We focus on the spin-down impurity as the spin-up impurity results are the same. The dynamics of such a locally quenched state can be used to compute the impurity Green's function.

As an initial test of the idea of disentangling dynamics using Gaussian circuits, we consider the non-interacting,  $U = 0$  case only in this work. This choice allows us to obtain precise results to arbitrary times. In contrast, studying the interacting dynamics in the transformed basis would require using the time-dependent variational principle (TDVP) algorithm [52, 53], which can experience convergence issues when the MPS bond dimension becomes small, such as after a disentangling transformation, and requires additional subspace expansion techniques. Therefore we leave the interacting case to a future work. Because entanglement behaves very similarly between interacting and non-interacting systems, we believe the results below are typical and do not depend on non-interacting physics in any special way.

Since the fermionic Gaussian state is fully characterized by the correlation matrix, the time evolution operator for the non-interacting system,  $U(t) = e^{-iht}$ , can be considered just a change of single-particle basis on the correlation matrix. Here  $h$  is the matrix of the single-particle Hamiltonian coefficients from Eq. 1. Thus, at

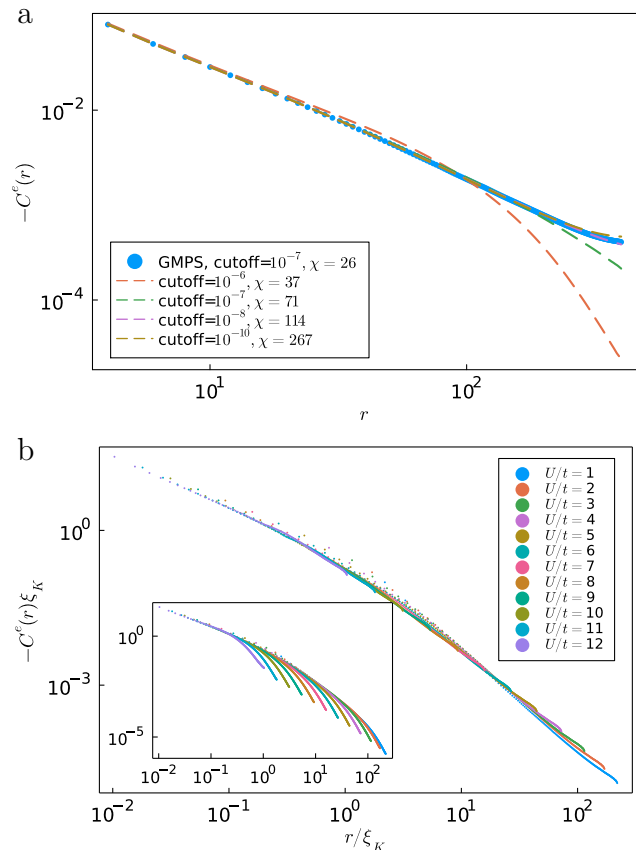


FIG. 6. Even site spin-spin correlator  $C^e(r)$  (Eq. 19) and the scaling collapse for  $N = 400, V = t, \epsilon_d = -U/2$  with various  $U \in [1, 12]$ . Empirically, the screening length is found to be  $\xi_K = e^{0.6U}/\sqrt{U}$ . (a) The correlation function  $C(r)$  with  $U = 10t$  from the DMRG in the GMPS transformed basis (solid circles) and in the original basis with various DMRG calculation cutoffs (dashed curves). (b) The correlation function  $C(r)$  first obtained from the DMRG algorithm in the GMPS transformed basis and then transformed back to the original basis with the DMRG calculation cutoff =  $10^{-6}$ . Inset: results in the original basis with the same axes, parameters and DMRG calculation cutoff.

any time  $t$ , the state can be fully represented by another correlation matrix

$$[\Lambda_q(t)]_{ij} = [U(t)\Lambda_q(0)U^\dagger(t)]_{ij}, \quad (22)$$

where  $[\Lambda_q(0)]_{ij} = \langle \Phi_0 | c_i^\dagger c_j | \Phi_0 \rangle$  and  $[\Lambda_q(t)]_{ij} = \langle \Phi(t) | c_i^\dagger c_j | \Phi(t) \rangle$ . Any correlation matrix of a fermionic Gaussian state with low enough entanglement can also be efficiently compressed into an MPS with a fermionic Gaussian circuit. The entanglement entropy for the quenched state is denoted as

$$S(r, t) = -\text{Tr}[\rho_r(t) \ln \rho_r(t)], \quad (23)$$

where  $\rho_r(t) = \text{Tr}_{\bar{r}} \rho, \rho = |\Phi(t)\rangle \langle \Phi(t)|$  and  $\text{Tr}_{\bar{r}}$  denotes trace over complement sites from  $r + 1$  to  $N$ . Note



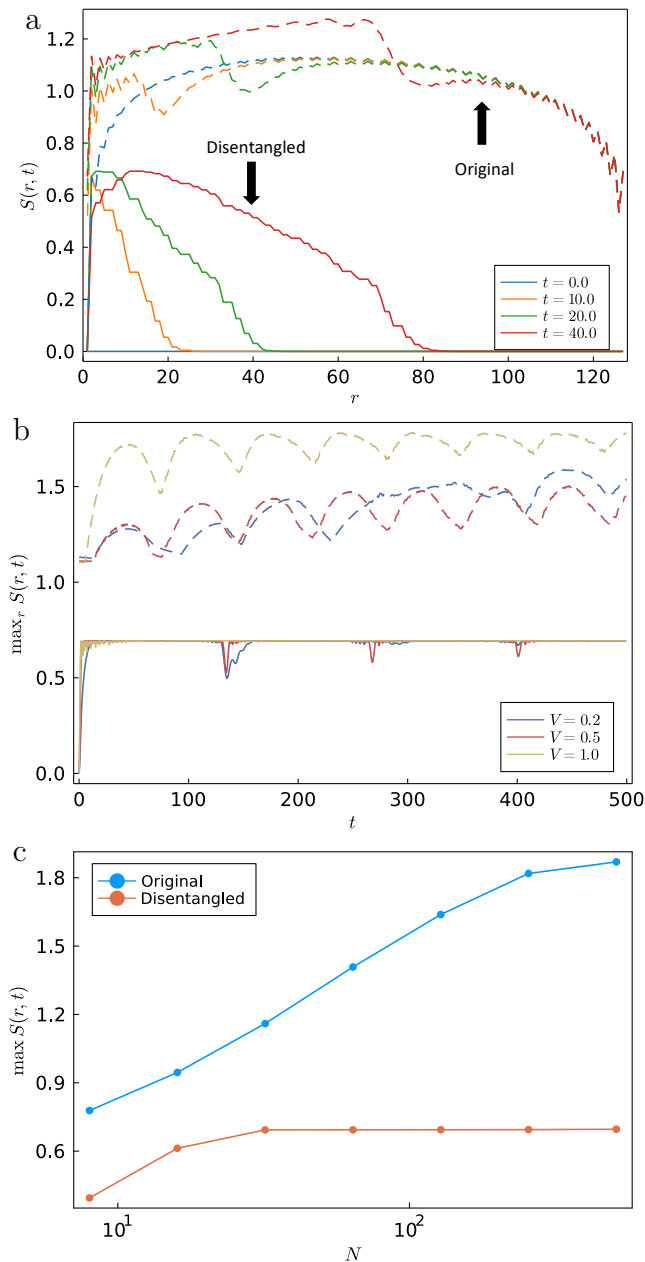


FIG. 7. The entanglement entropy of the quenched non-interacting system. (a) The entanglement entropy as a function of bipartite sites for several time snapshot for system size  $N = 128, V = 0.2t$ . Solid curves are the entanglement after applying the GMPS circuit (disentangled) while dashed curves are the original basis results. (b) The maximum entanglement entropy (across sites) as a function of time with  $N = 128$ . Solid curves are results in the GMPS basis while dashed curves are the original. (c) The time averaged maximum entanglement entropy (over various  $t$  range with 100 data points) as a function of system size  $N$  with  $V = 0.2t$ .

that the entanglement entropy can be computed directly from the correlation matrix in a straightforward way (Appendix A of [16]).

Fig. 7 shows the behavior of the entanglement entropy for the time-evolved quenched state  $|\Phi(t)\rangle$ . Panel (a) shows four snapshots of the entanglement structure. Note that at time  $t = 0$ , the quenched state  $|\Phi(0)\rangle$  has almost no entanglement after applying the GMPS circuit from the ground state. As the state evolves, the transformed-basis entanglement grows outward from the impurity and spreads across further sites. Interestingly, the region where the transformed-basis entanglement is non-zero corresponds to where the original-basis entanglement deviates from its time  $t = 0$  value.

In Fig. 7(b) we focus on the maximum value of entanglement across all sites and plot its time dependence. In the original basis, the entanglement starts at a relatively large value around 1.1 and grows to 1.5, where it saturates. (The oscillations are finite-size effects and occur at multiples of the system size.) In contrast, in the transformed basis the maximum entanglement starts out very small at early times then becomes nearly constant (0.69) at late times, at a value much lower than the original-basis entanglement. The disentangling power of the circuit is even more prominent when we look at the system size scaling of the maximum entanglement in panel (c), which is averaged over time to smooth the finite size oscillations. The GMPS circuit not only decreases the overall entanglement but also keeps the growth of entanglement with system size under control. Our results demonstrate that fermionic Gaussian circuits could be a powerful tool to compute the unitary time evolution in interacting systems, though we leave this for future work.

## VII. ENTANGLEMENT RENORMALIZATION OF THE BATH ELECTRONS

In the sections above, we considered fermionic Gaussian circuits with the structure of the GMPS, which worked very well in disentangling the interacting problem with local orbitals. However, the large degeneracy of the correlation matrix eigenvalues gives us freedom to choose other diagonalization procedures. In this section, we introduce other types of fermionic Gaussian circuits with structures inspired by the multi-scale entanglement renormalization ansatz (MERA) and discuss how the transformed Hamiltonians have interesting emergent properties in the context of finding ground state energies and performing time evolution.

### A. GMERA and Emergent Models

By introducing non-local unitary gates with a hierarchical structure, a class of fermionic Gaussian circuits implementing the MERA tensor network structure were proposed in Ref. 21 and a simplified construction was introduced in Ref. 16. This fermionic Gaussian circuit is called the Gaussian MERA (GMERA) circuit, and its construction can be conveniently realized as a simple

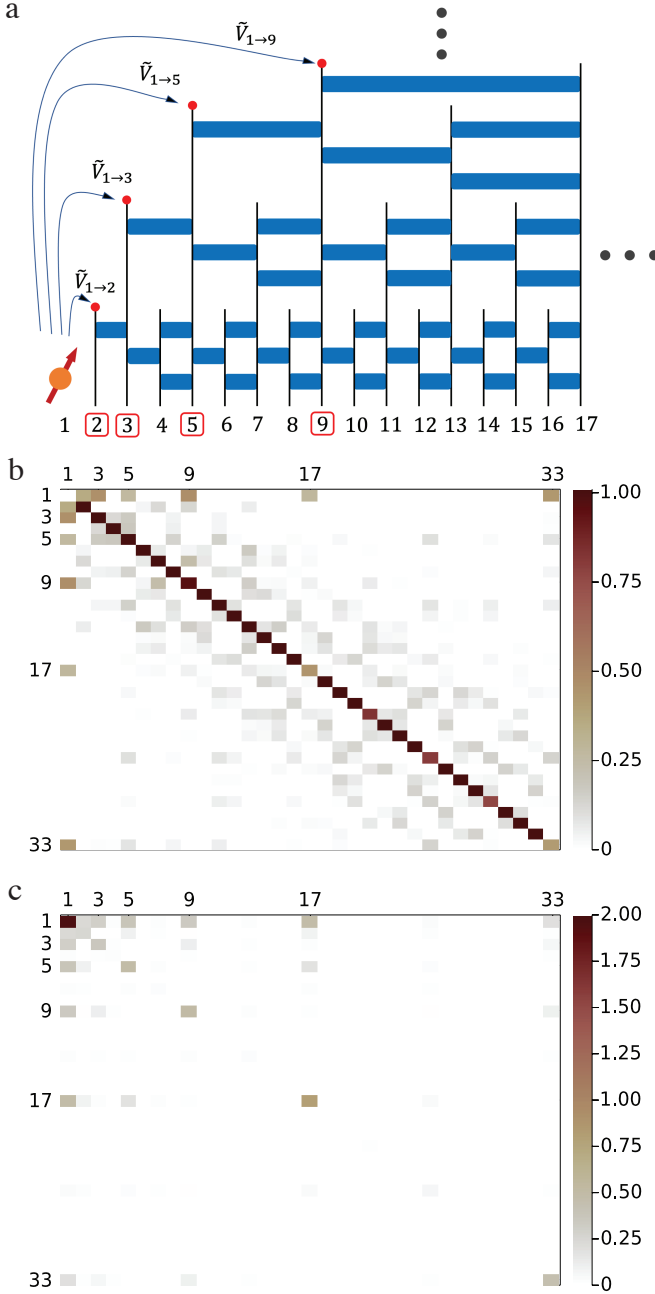


FIG. 8. Demonstration of the GMERA circuit. (a) the GMERA circuit obtained by diagonalizing odd sites in each iteration with system size  $N = 16$  and block size  $B = 4$ . The impurity acts as a local spin in the left. The GMERA circuit generates effective hybridizations from the impurity to exponential sites,  $r = 2^k + 1, k = 0, 1, \dots$ , marked by the red dots and red squares. (b) The transformed hopping Hamiltonian ( $U = 0$ ) under the GMERA circuit from the bath electrons with  $N = 80, V = t$ , where the effective hybridizations (color bar) are prominent. (c) The part of mutual information matrix  $I(r_1, r_2)$  of the ground state with  $U = t$  for  $N = 80, V = t$ . The peaks (color bar) in the mutual information perfectly fit with exponential sites appeared in (a) and (b).

modification of the GMPS circuit construction where the gates are reorganized into a hierarchical structure. (The GMERA circuits are closely related to “deep MERA” circuits [54, 55] but are composed of Gaussian matchgates Eq. (7).) In contrast to the GMPS circuit which constructs a single layer of gates in one long pass over the system, the GMERA circuit makes a logarithmic number of passes over the system as shown in Fig. 8(a). In this way, higher layers of the circuit introduce longer-range basis transformations in real space, capturing longer-range correlations.

Here we are primarily interested in how the entanglement-based renormalization group carried out by the GMERA coarse grains the impurity problem and gives rise to an emergent effective Hamiltonian with fewer degrees of freedom, in one case resembling a Wilson chain from the numerical renormalization group approach. Similar to the GMPS construction, we only apply the GMERA circuit to the bath electrons as shown in Fig. 8(a) in order to avoid spreading the interaction terms over multiple sites in the transformed basis.

In each layer/iteration, a GMERA circuit starts from the bath sites closest to the impurity, whose real space location scales exponentially as  $r = 2, 3, 5, \dots$  (or  $r = 2^k + 1$  with  $k = 0, 1, 2, \dots$ ). The entanglement renormalization generates effective *bath hybridizations* directly from the impurity to these logarithmic number of sites, reflected by the first row and column in the GMERA-transformed bath in Fig. 8(b).

The most significant hopping terms in the transformed bath form a pattern resembling the so-called “star geometry” form of an impurity problem [23, 24]

$$H_{\text{eff}}^{\text{star}} \equiv H_{\text{imp}} + \sum_{k \in \mathcal{A}, \sigma} \left[ \tilde{V}_k (d_{\sigma}^{\dagger} c_{k\sigma} + \text{H.c.}) + \tilde{\varepsilon}_k c_{k\sigma}^{\dagger} c_{k\sigma} \right], \quad (24)$$

where there are no hoppings between bath sites and only hybridizations  $\tilde{V}_k$  to the impurity site. Here  $k$  denotes the GMERA orbitals that run over the set  $\mathcal{A}$  of coarse-grained active orbitals that are strongly entangled with the impurity. The matrix elements  $\tilde{\varepsilon}_k, \tilde{V}_k$  are the transformed bath couplings to the impurity, that is, the diagonal and the first row of Fig. 8(b).

Since the entanglement renormalization procedure does not project out diagonal components of the Hamiltonian, the inactive (diagonal) set of orbitals,  $\mathcal{I}$ , needs to be included explicitly as

$$H_{\text{eff}}^{\text{GMERA}} = H_{\text{eff}}^{\text{star}} + \sum_{k \in \mathcal{I}, \sigma} \tilde{\varepsilon}_k c_{k\sigma}^{\dagger} c_{k\sigma}, \quad (25)$$

for the ground state energy to be preserved.

The decoupling of the complementary sites from the impurity can be further verified by computing the mutual information matrix, which is defined as

$$I(r_1, r_2) = S(\rho_{\{r_1\}}) + S(\rho_{\{r_2\}}) - S(\rho_{\{r_1, r_2\}}), \quad (26)$$

where  $\rho_{\{\dots\}}$  denotes the reduced density matrix for the sites specified inside the curly brackets. In Fig. 8(c), numerical results including a non-zero interaction  $U$  indicate that the mutual information is strongly peaked at these exponential sites while the majority of the remaining sites share negligible mutual information with the impurity [56].

An interesting variation of the GMERA circuit is to omit the part of each layer closest to the impurity, as shown in Fig. 9(a). We call this pattern the boundary GMERA (bGMERA) circuit. This is reminiscent of the boundary MERA introduced in Ref. 25–27, a modification of the traditional MERA tensor networks in the presence of boundaries and impurities. Instead of fully diagonalizing the correlation matrix, this procedure intentionally keeps the first site in each iteration untreated. These untreated sites also scale exponentially in distance in the transformed basis,  $r = 2^k$ , with  $k = 1, 2, \dots$  and create long-range hopping in the transformed bath Hamiltonian as shown in Fig. 9(b). The pattern from the transformed Hamiltonian provides a coarse-grained version of the chain-like geometry of the original model (Eq. 8,  $H^{\text{chain}} = H_A$ )

$$H_{\text{eff}}^{\text{chain}} = H_{\text{imp}} + \sum_{\sigma} \left[ \tilde{V}(d_{\sigma}^{\dagger} c_{2\sigma} + \text{H.c.}) + \tilde{\varepsilon}_2 c_{2\sigma}^{\dagger} c_{2\sigma} \right] + \sum_{k \in \mathcal{A}, \sigma} \left[ \tilde{t}_k (c_{k\sigma}^{\dagger} c_{k+1\sigma} + \text{H.c.}) + \tilde{\varepsilon}_{k+1} c_{k+1\sigma}^{\dagger} c_{k+1\sigma} \right], \quad (27)$$

where  $k$  is the boundary GMERA orbitals and the set  $\mathcal{A}$  is the set of coarse-grained active orbitals from boundary GMERA. The transformed hybridization  $\tilde{V}$  and matrix elements  $\tilde{\varepsilon}_k, \tilde{t}_k$  can be read out from the transformed quadratic part of the Hamiltonian, i.e., the diagonal and the prominent hopping at sites  $2^k$  of Fig. 9(b). Again, for the energy to match the original, untransformed system, the inactive complementary set of orbitals,  $\mathcal{I}$  have a purely diagonal Hamiltonian which we can add to form the total Hamiltonian as

$$H_{\text{eff}}^{\text{bGMERA}} = H_{\text{eff}}^{\text{chain}} + \sum_{k \in \mathcal{I}, \sigma} \tilde{\varepsilon}_k c_{k\sigma}^{\dagger} c_{k\sigma}. \quad (28)$$

The mutual information, shown in Fig. 9(c), elucidates the pattern of correlations between the active and inactive orbitals and the impurity. This is consistent with previous results on boundary MERA where a Wilson-chain-like structure [57] naturally arises from the MERA tensor network in the presence of impurities [25–27]. Here we also find the emergent long-range hopping terms (significant off-diagonal entries in Fig. 9(b)) also form a chain of hoppings between the active sites, with values decaying with distance from the impurity. We plan to investigate the connection to the Wilson chain construction in more depth in a future work.

The correctness of the above two emergent reduced effective Hamiltonians for approximating the ground-state energy is surprisingly good, as shown in Fig. 10.

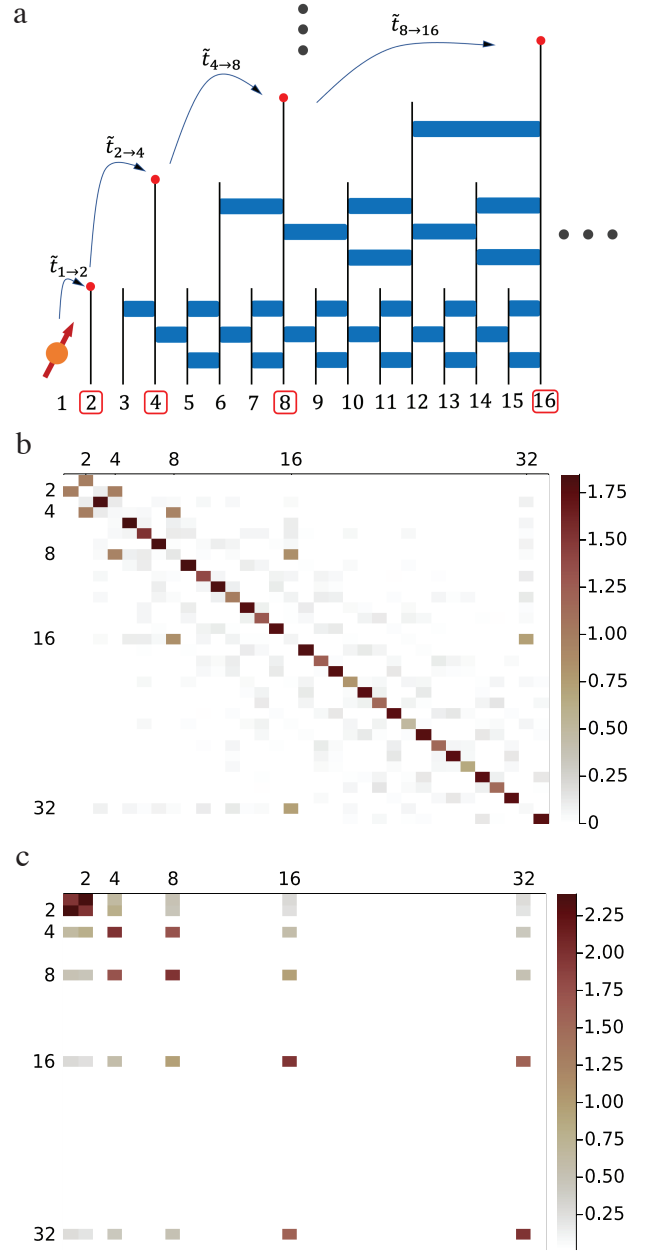


FIG. 9. Demonstration of a boundary GMERA circuit. (a) the boundary GMERA circuit obtained by diagonalizing even sites in each iteration with system size  $N = 16$  and block size  $B = 4$ . The impurity acts as a local spin in the left. The boundary GMERA circuit generates long-range hoppings among exponential sites,  $r = 2^k, k = 0, 1, \dots$ , marked by the red dots and red squares. (b) The transformed bath Hamiltonian under the boundary GMERA circuit from bath electrons with  $N = 80, V = t$ , where the effective hoppings (color bar) are prominent. (c) The part of mutual information matrix  $I(r_1, r_2)$  of the ground state with  $U = t$  for  $N = 80, V = t$ . The peaks in the mutual information (color bar) perfectly fit with exponential sites appeared in (a) and (b).

For a system of size  $N = 129$ , a reduced system of

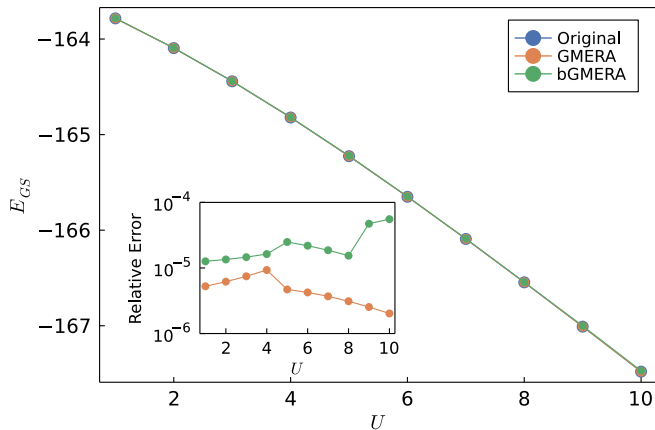


FIG. 10. The ground state energy as a function of interaction strength  $U$  with  $N = 129, V = t, \epsilon_d = -U/2$ . The GMERA energies are obtained by finding the ground state in the emergent Hamiltonian,  $H_{\text{eff}}^{\text{chain}}, H_{\text{eff}}^{\text{star}}$ , plus single-particle energies smaller than the chemical potential,  $\mu = 0$ . The relevant sites are  $N_{\text{GMERA}} = 22, N_{\text{bGMERA}} = 14$ , respectively, which are selected from the mutual information with cutoff  $I(1, r) \geq 10^{-3}$ . Inset: the relative error of the emergent Hamiltonian benchmarked by the ground state in the original basis.

$N_{\text{bGMERA}} = 14$  sites can already accurately capture the ground state energy for a wide range of interactions  $U/t \in [1, 10]$  with an error less than 0.1% [58]. Note that such great agreement of ground state energies is not obvious purely from the transformed bath Hamiltonian since some neglected terms of the Hamiltonian have coefficients with absolute values greater than 0.1. Thus, entanglement renormalization of the GMERA circuits yield non-trivial emergent models for the interacting problem.

### B. Time Evolution under the GMERA Gates

Another application of the GMERA circuits is to time evolve the quenched state  $|\Phi(t)\rangle$  from Eq. 21 and compare the impurity Green's function in the coarse-grained models

$$\begin{aligned} G_{\downarrow}(t) &\equiv \langle d_{\downarrow}^{\dagger}(t) d_{\downarrow}(0) \rangle \\ &= e^{iE_0 t/\hbar} \langle \Psi_0 | d_{\downarrow}^{\dagger} U(t) d_{\downarrow} | \Psi_0 \rangle \\ &= e^{iE_0 t/\hbar} \langle \Phi(0) | \Phi(t) \rangle, \end{aligned} \quad (29)$$

where  $E_0$  is the energy of the ground state. This is an important quantity both for understanding impurity physics and as an input to the dynamical mean-field theory (DMFT) method [59]. We still focus on time evolving non-interacting impurity models as in Section VI. Previously, the emergent active sites were identified by analyzing the mutual information of ground states. Though the ground state shares very similar mutual information peaks with the impurity quenched state at most times

[60], we find it is more accurate to obtain emergent sites from the quenched state mutual information.

The dynamics of the impurity Green's function, Eq. 29, is shown in Fig. 11. Given the same system size  $N$ , the absolute values of  $|G_{\downarrow}(t)|$  are invariant under arbitrary unitary change of basis. In other words,  $|G_{\downarrow}(t)|$  stays the same for the GMPS, the GMERA and the boundary GMERA circuits without coarse-graining. However, if we choose to only work with the active sites  $\mathcal{A}$  (from Eqs. 24 and 27) based on the mutual information of  $|\Phi(t)\rangle$  at a typical time, e.g.  $t = 10$ , and time evolve the impurity under the resulting emergent Hamiltonian, the impurity Green's function can be well approximated with an exponentially small system size ( $N_{\text{GMERA}} = 45, N_{\text{bGMERA}} = 28$  as compared to the full size  $N = 256$ ) for a wide range of time until finite size effects start to dominate. Unlike calculating the ground state energies, the inactive sites (sites with occupancies very close to 0 or 1) only provide a phase change in their eigenstates, which cancel out for the expectation value of the Green's function and thus are irrelevant [61]. The fact that the Green's function can be obtained through a logarithmically small system makes GMERA and boundary GMERA circuits a powerful tools for dynamics, though their efficacy is yet to be seen for studying the dynamics of interacting systems.

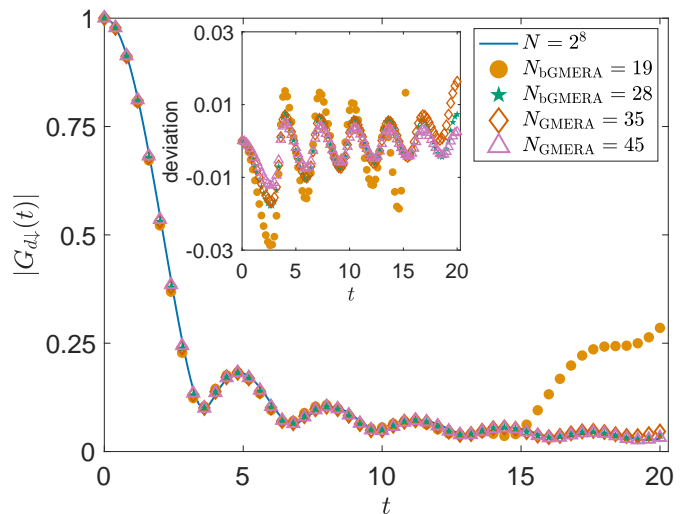


FIG. 11. The dynamics of the impurity Green's function (Eq. 29) for emergent Hamiltonians with original system  $N = 256, V = t$ . The blue solid curve represents the Green's function with the full size regardless of basis. The different markers are emergent systems from GMERA (empty markers) and boundary GMERA (bGMERA, solid markers) transformed basis, which is taken from the mutual information of the quenched state  $|\Phi(t = 10)\rangle$ . For each case, the two different emergent system sizes (that are labeled in the legend) are obtained at two mutual information cutoffs ( $10^{-4}$  and  $10^{-5}$ ). Inset: the deviation of the emergent models away from the full system Green's function.

### VIII. CONCLUSION AND DISCUSSION

Fermionic Gaussian circuits obtained from non-interacting states can drastically reduce the entanglement of the interacting single-impurity Anderson model. Circuits known as Gaussian matrix product states (GMPS) are able to efficiently disentangle many-body ground states across a wide range of interactions realizing different fixed-point physics of the impurity problem. Furthermore, transforming the Hamiltonian before performing a DMRG calculation can yield much faster DMRG runtimes and more accurate properties for a given truncation threshold.

We studied the Kondo screening cloud under the GMPS circuit transformation, finding the entanglement remaining after a GMPS transformation harbors universal information about Kondo screening physics. We also studied the potential for GMPS transformations to reduce the entanglement of systems undergoing dynamics, where the entanglement growth of a quenched, non-interacting system was found to hardly increase with system size after the transformation, in stark contrast to the behavior in the original real space basis.

We then tested a variation of fermionic Gaussian circuits inspired by the multi-scale entanglement renormalization ansatz (MERA) tensor network, called the fermionic Gaussian MERA (GMERA). Such a renormalization introduces a hierarchical structure which induces effective long-range interactions. In this renormalized basis an effective reduced system is identified which is comprised of a logarithmic number of sites that are highly entangled to the impurity (or each other, depending on the construction), from which a smaller effective Hamiltonian emerges and the rest of the sites can be treated as decoupled free electron modes. Such a bold approximation works exceptionally well in finding the ground state energies for a wide range of interactions and can also efficiently simulate the impurity Green's function dynamics, over a time range subjected to finite size effect. The essential functionalities for conveniently working with fermionic Gaussian circuits are now available in the Julia ITensor ecosystem [62].

There are many more directions to explore in applying fermionic Gaussian circuit transformations to interacting systems. A direct extension of the current work is to study the effects of using the GMPS circuit as a basis transformation when time evolving interacting impurity problems with modern time evolution methods able to handle the complicated transformed Hamiltonian. Based on the results from non-interacting systems, we believe GMPS circuits could also keep entanglement of the interacting problem under control. When using the GMERA circuit, it will be interesting to see how well the emergent sites from non-interacting quenched states still work in time evolution when including interactions. In a separate but related vein, recent work has demonstrated how to efficiently convert the so-called influence matrix in time evolution of interacting impurity models

[34], which shows a potential usage of fermionic Gaussian circuits in non-equilibrium quantum dynamics under non-interacting fermionic reservoirs.

Some more challenging directions involve uniformly interacting systems, such as in the one-dimensional Hubbard model, where the locality of the interaction could be crucial. In general, we believe the application of fermionic Gaussian circuits could push tensor network methods and DMRG toward handling much more challenging and highly-entangled problems with a proper choice of the fermionic Gaussian circuit transformation, potentially even in higher dimensions, i.e., general tree tensor networks, MERA circuits in 2D systems and Gaussian projected entangled pair states for 2D fermionic problems.

### ACKNOWLEDGEMENTS

We thank Xiaodong Cao, Chia-Min Chung, Jan von Delft, Örs Legeza, Olivier Parcollet, and Andreas Weichselbaum for constructive discussions. All calculations were performed with the ITensor software [40, 63] in the Julia language [64]. A.-K. W. and J.H.P. are partially supported by National Science Foundation (NSF) CAREER Grant No. DMR-1941569 and the Alfred P. Sloan Foundation through a Sloan Research Fellowship.

### Appendix A: Split-site Representation

In Sec. III we introduced the split spin representation of the Anderson impurity model, here in this Appendix we describe this in more detail. Without changing the physics, the impurity model can be rewritten by separating the spin up and down operators  $a_{-j} \equiv c_{j\uparrow}$ ,  $a_j \equiv c_{j\downarrow}$ , which has been used often for studying impurity systems with MPS techniques [35–38].

Specifically, the model can be rewritten in terms of spinless fermion operators by putting all up spins on the left side of the impurity and all down spins on the right side. The impurity becomes two spinless fermion sites in the center of the system. Quantitatively:

$$H_A = H_\uparrow + H_{\text{imp}} + H_\downarrow, \quad (\text{A1})$$

with

$$\begin{aligned} H_\uparrow &= -t \sum_{j=-2}^{-(N-1)} (a_j^\dagger a_{j-1} + \text{H.c.}) - V(a_{-1}^\dagger a_{-2} + \text{H.c.}) \\ H_{\text{imp}} &= \epsilon_d(\hat{n}_{-1} + \hat{n}_1) + U\hat{n}_{-1}\hat{n}_1 \\ H_\downarrow &= -V(a_1^\dagger a_2 + \text{H.c.}) - t \sum_{j=2}^{N-1} (a_j^\dagger a_{j+1} + \text{H.c.}). \end{aligned} \quad (\text{A2})$$

Here  $a_j$  is a spinless fermionic operator.  $j < 0$  represents original site  $r = -j$  for up spins while  $j > 0$  is site  $r = j$

for down spins, and  $-1, 1$  sites are the impurity site for up and down impurity spins (index 0 is skipped).  $\hat{n}_j = a_j^\dagger a_j$  is the occupancy operator. For all cases, we keep the particle-hole symmetry for the impurity  $U = -2\epsilon_d$ .

As alluded to earlier, the primary advantage of this model geometry is that the ground state bond dimension  $\chi$  is decreased by approximately square root of the original bond dimension (which becomes exact in the non-interacting limit  $U = 0$ ) for the same MPS accuracy. The trade-off is that computing operators such as the spin-spin correlators  $C(r) = \langle \mathbf{S}(1) \cdot \mathbf{S}(r) \rangle$  and the bipartite impurity entanglement entropy  $S(r)$  in real space become slightly more complicated to compute.

### Appendix B: Entanglement entropy of a middle segment in an MPS (ABA partition)

To obtain the entanglement entropy of a cloud of radius  $r$  around the impurity in real space, we need to divide the split-site geometry of the 1D chain into three partitions, where the entanglement entropy of interest is between the middle partition of sites  $j \in [-r, r]$  and the rest of the system. The orthogonality or the canonical form of the MPS is crucial in obtaining the entanglement of this ABA partition. To begin with, it is helpful to revisit how the bipartite entanglement is computed. When we decompose a 1D chain into blocks of  $A$  and  $B$ , where block  $A$  goes from 1 to  $l$  while  $B$  goes from  $l+1$  to  $N$ , we can order the MPS in the following way

$$\begin{aligned} |\Psi_0\rangle &= \sum_{\sigma_1, \dots, \sigma_{2N}} c_{\sigma_1, \dots, \sigma_{2N}} |\sigma_1, \dots, \sigma_{2N}\rangle \\ &= \sum_{\sigma_1, \dots, \sigma_{2N}} M^{\sigma_1} M^{\sigma_2} \dots M^{\sigma_{2N}} |\sigma_1, \dots, \sigma_{2N}\rangle \quad (\text{B1}) \\ &= \sum_{a_l} |a_l\rangle_A |a_l\rangle_B, \end{aligned}$$

where

$$\begin{aligned} |a_l\rangle_A &= \sum_{\sigma_1, \dots, \sigma_l} (M^{\sigma_1} \dots M^{\sigma_l})_{1, a_l} |\sigma_1, \dots, \sigma_l\rangle, \\ |a_l\rangle_B &= \sum_{\sigma_{l+1}, \dots, \sigma_N} (M^{\sigma_{l+1}} \dots M^{\sigma_N})_{a_l, 1} |\sigma_{l+1}, \dots, \sigma_N\rangle. \end{aligned} \quad (\text{B2})$$

The boundary tensors  $M^{\sigma_1}, M^{\sigma_N}$  give 1 in the subscript. Note that this decomposition  $|\Psi_0\rangle = \sum_{a_l} |a_l\rangle_A |a_l\rangle_B$  is not a Schmidt decomposition, because, in the left-canonical form of  $M^\sigma$ , the states  $|a_l\rangle_A$  form an orthonormal set for system  $A$  while states  $|a_l\rangle_B$  do not. Thus, to perform the Schmidt decomposition, we apply the singular value decomposition (SVD) to the index/bond between  $M^{\sigma_l}$  and  $M^{\sigma_{l+1}}$ , where the diagonal  $S$  matrix gives the singular values.

For the ABA partition, where the middle part runs from  $l_1+1$  to  $l_2$ , we want to use a mixed-canonical MPS

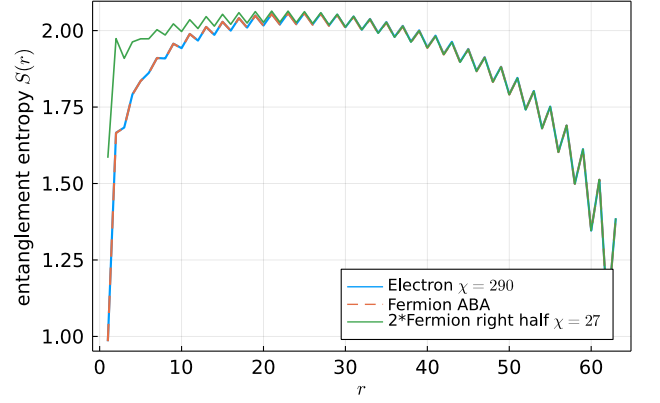


FIG. 12. Entanglement entropy in different geometries of the single impurity Anderson model with  $N = 64, V = 1.0t, U = 8t, \epsilon_d = -U/2$ . Solid blue curve represents bipartite entropy in the electron name space of the Hamiltonian where the impurity locates in the left. Red dashed curve is the entanglement entropy of a middle segment of the split-site MPS with a radius  $r$  around the impurity sites. Green curve is the double of the right half of the bipartite entropy of the split-site MPS, demonstrating that it is quantitatively similar to the electron entanglement entropy sufficiently far from the impurity.

automatically facilitated by ITensor, which allows us to represent the wavefunction amplitudes in Eq. (B1) as

$$c_{\sigma_1, \dots, \sigma_N} = \sum_{\sigma_1, \dots, \sigma_N} L^{\sigma_1} \dots L^{\sigma_{l_1}} S R^{\sigma_{l_1+1}} \dots R^{\sigma_N}, \quad (\text{B3})$$

where  $L^\sigma, R^\sigma$  represent left and right normalized,  $\sum_\sigma (L^\sigma)^\dagger L^\sigma = \sum_\sigma R^\sigma (R^\sigma)^\dagger = \mathbb{I}$  respectively with the orthogonality center at site  $l_1 + 1$ . The decomposition we look for is

$$\begin{aligned} |\Psi_0\rangle &= \sum_b |a\rangle_A |b\rangle_B |c\rangle_C, \\ |a\rangle_A &= \sum_{\sigma_1, \dots, \sigma_{l_1}} (L^{\sigma_1} \dots L^{\sigma_{l_1}})_{1, a} |\sigma_1, \dots, \sigma_{l_1}\rangle, \\ |b\rangle_B &= \sum_{\sigma_{l_1+1}, \dots, \sigma_{l_2}} (S R^{\sigma_{l_1+1}} \dots R^{\sigma_{l_2}})_{a, c} |\sigma_{l_1+1}, \dots, \sigma_{l_2}\rangle, \\ |c\rangle_C &= \sum_{\sigma_{l_2+1}, \dots, \sigma_N} (R^{\sigma_{l_2+1}} \dots R^{\sigma_N})_{c, 1} |\sigma_{l_2+1}, \dots, \sigma_N\rangle, \end{aligned} \quad (\text{B4})$$

where for both subsystem  $A$  and  $C$ , the states are orthogonal and states  $|b\rangle_B$  will have a size of  $a \times c$ . However, if we directly extract the middle segment, we will still work on a huge tensor with physical space  $2^{l_2-l_1}$  for the SVD while most information within the middle segment is redundant. Therefore, we can instead contract these physical indexes  $l_1+1, \dots, l_2$  but only leave the 2 bond indexes by multiplying with complex conjugate of  $|b\rangle_B$  as the compressed density matrix. In the end, the SVD will work on a reduced tensor, consisting of 4 indices

$a, a', c, c'$ , by 2 indices  $a, c$ . Graphic instructions for this calculation appear in the Appendix A of Ref. 65.

When comparing the split-site representation of the Hamiltonian with the original electron representation as in Fig. 12, it is clear that the bipartite entanglement entropy in the electron space is the same as the middle segment entropy of the split-site MPS. Sufficiently far away from the impurity, the entanglement entropy is well described by twice that of the split-site fermion MPS.

### Appendix C: Variations of the GMPS circuits

In the main text, the GMPS circuits are obtained from the  $U = 0$  limit of the impurity model (known as the resonant level model, RLM) with impurity gates dropped so as to maintain locality of the Coulomb repulsion  $U$ . Such a treatment benefits the computation without changing the qualitative disentangling behavior. As shown in Fig. 13, the disentangled results are very similar between the circuits with and without gates involving the impurity. Though, the full circuit gives less entanglement at the impurity site in the small  $U$  limit, the entanglements away from the impurity are basically

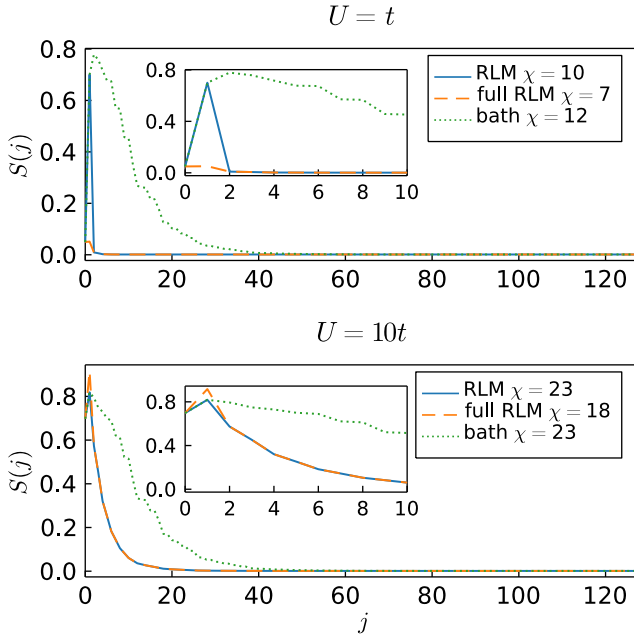


FIG. 13. Disentangling effect of different GMPS circuits for system  $N = 128, V = t$  for the small repulsion  $U = t$  (upper panel) and the large repulsion  $U = 10t$  (lower panel) cases. The solid curves are the same results as the main text disentangled by the GMPS circuit from the resonant level model with impurity gates dropped in the end. The orange dashed curves are results under the whole GMPS circuit without dropping gates. The green dotted curves are results under the GMPS circuit obtained only from bath electrons.

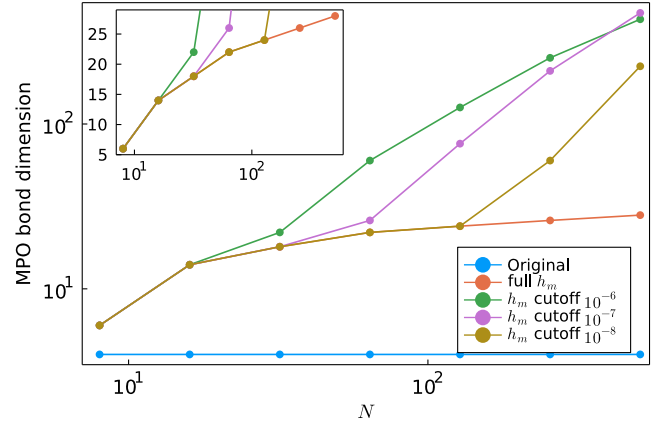


FIG. 14. The maximum bond dimensions  $\chi$  as a function of physical sizes  $N$  with various hopping cutoffs with  $V = t, U = t$ . Given a finite cutoff, the maximum MPO bond  $\chi$  dramatically increases at a large system size. Inset: same results in log- $x$  scale.

the same with the circuit that avoids the impurity, which becomes more prominent in large  $U$  limit.

The GMPS circuit obtained from the bath electrons is also considered in Fig. 13. Compared to the resonant level model, disentangling results of the circuit from the bath has higher entanglement over a large range of sites around the impurity. Qualitatively, we attribute this to the electron MPS having to represent the impurity bound state as a superposition over a large number of bath sites, which is already taken into account exactly in the resonant level model MPS.

### Appendix D: Hamiltonian MPO with hopping cutoff

In Sec. IV B of the main text, the GMPS circuits are used to transform the Hamiltonian, which generate quadratic number of terms. To constrain the number of non-zero hopping terms  $t_{kl}$  in the transformed non-interacting Hamiltonian,  $\tilde{H}_\uparrow = R^\dagger H_\uparrow R = \sum_{kl} t_{kl} f_k^\dagger f_l$ , we tried imposing a hopping size cutoff, whose effects on the resulting compressed MPO are studied here. As shown in Fig. 14, the maximum MPO bond dimensions does not change with system sizes in the original basis, while it increases logarithmically in the system size  $N$  asymptotically when we use all non-zero terms in the transformed basis. Perhaps counterintuitively, attempting to truncate small hopping terms according to a fixed cutoff leads to MPOs with larger bond dimensions. Thus, small hopping terms have non-trivial contribution in compressing the Hamiltonian into an MPO. This effect can possibly be understood as the hoppings having a smooth decaying behavior, so that truncating them introduces artificial “steps” that can make the MPO compression algorithm less effective. Therefore in practice

we keep all transformed Hamiltonian terms.

- 
- [1] S. R. White, *Phys. Rev. Lett.* **69**, 2863 (1992).
- [2] S. R. White, *Phys. Rev. B* **48**, 10345 (1993).
- [3] U. Schollwöck, *Rev. Mod. Phys.* **77**, 259 (2005).
- [4] K. A. Hallberg, *Adv. Phys.* **55**, 477 (2006).
- [5] U. Schollwöck, *Ann. Phys.* **326**, 96 (2011).
- [6] G. Evenbly and G. Vidal, *J. Stat. Phys.* **145**, 891 (2011).
- [7] T. Barthel, M.-C. Chung, and U. Schollwöck, *Phys. Rev. A* **74**, 022329 (2006).
- [8] M. M. Wolf, *Phys. Rev. Lett.* **96**, 010404 (2006).
- [9] L. Vidmar, L. Hackl, E. Bianchi, and M. Rigol, *Phys. Rev. Lett.* **119**, 020601 (2017).
- [10] B. Bhattacharjee, P. Nandy, and T. Pathak, *Phys. Rev. B* **104**, 214306 (2021).
- [11] E. Bianchi, L. Hackl, and M. Kieburg, *Phys. Rev. B* **103**, L241118 (2021).
- [12] M. Kiefer-Emmanouilidis, R. Unanyan, J. Sirker, and M. Fleischhauer, *SciPost Phys.* **8**, 083 (2020).
- [13] C. Krumnow, L. Veis, O. Legeza, and J. Eisert, *Phys. Rev. Lett.* **117**, 210402 (2016).
- [14] C. Krumnow, J. Eisert, and Ö. Legeza, [arXiv:1904.11999](https://arxiv.org/abs/1904.11999) (2019).
- [15] C. Krumnow, L. Veis, J. Eisert, and O. Legeza, *Phys. Rev. B* **104**, 075137 (2021).
- [16] M. T. Fishman and S. R. White, *Phys. Rev. B* **92**, 075132 (2015).
- [17] S. Rommer and S. Östlund, *Phys. Rev. B* **55**, 2164 (1997).
- [18] Y.-Y. Shi, L.-M. Duan, and G. Vidal, *Phys. Rev. A* **74**, 022320 (2006).
- [19] G. Vidal, *Phys. Rev. Lett.* **99**, 220405 (2007).
- [20] G. Vidal, *Phys. Rev. Lett.* **101**, 110501 (2008).
- [21] G. Evenbly and G. Vidal, *Phys. Rev. B* **81**, 235102 (2010).
- [22] P. W. Anderson, *Phys. Rev.* **124**, 41 (1961).
- [23] D. Bauernfeind, M. Aichhorn, and H. G. Evertz, [arXiv:1906.09077](https://arxiv.org/abs/1906.09077) (2019).
- [24] F. A. Wolf, I. P. McCulloch, and U. Schollwöck, *Phys. Rev. B* **90**, 235131 (2014).
- [25] G. Evenbly, R. N. C. Pfeifer, V. Picó, S. Iblisdir, L. Tagliacozzo, I. P. McCulloch, and G. Vidal, *Phys. Rev. B* **82**, 161107 (2010).
- [26] G. Evenbly and G. Vidal, *J. Stat. Phys.* **157**, 931 (2014).
- [27] G. Evenbly and G. Vidal, *Phys. Rev. B* **91**, 205119 (2015).
- [28] K. G. Wilson, *Rev. Mod. Phys.* **47**, 773 (1975).
- [29] R. Bulla, T. A. Costi, and T. Pruschke, *Rev. Mod. Phys.* **80**, 395 (2008).
- [30] J. Surace and L. Tagliacozzo, *SciPost Phys. Lect. Notes* **54** (2022).
- [31] L. G. Valiant, *SIAM J. Comput.* **31**, 1229 (2002).
- [32] R. Jozsa and A. Miyake, *Proc. R. Soc. A* **464**, 3089 (2008).
- [33] G. Vidal, J. I. Latorre, E. Rico, and A. Kitaev, *Phys. Rev. Lett.* **90**, 227902 (2003).
- [34] J. Thoenniss, A. Lerose, and D. A. Abanin, [arXiv:2205.04995](https://arxiv.org/abs/2205.04995) (2022).
- [35] H. Saberi, A. Weichselbaum, and J. von Delft, *Phys. Rev. B* **78**, 035124 (2008).
- [36] M. Ganahl, M. Aichhorn, H. G. Evertz, P. Thunström, K. Held, and F. Verstraete, *Phys. Rev. B* **92**, 155132 (2015).
- [37] M. M. Rams and M. Zwolak, *Phys. Rev. Lett.* **124**, 137701 (2020).
- [38] L. Kohn and G. E. Santoro, *Phys. Rev. B* **104**, 014303 (2021).
- [39] G. K.-L. Chan, A. Keselman, N. Nakatani, Z. Li, and S. R. White, *J. Chem. Phys.* **145**, 014102 (2016).
- [40] M. Fishman, S. R. White, and E. M. Stoudenmire, *SciPost Phys. Codebases*, 4 (2022).
- [41] A. C. Hewson, *The Kondo Problem to Heavy Fermions* (Cambridge University Press, Cambridge, UK, 1993).
- [42] S. Boutin and B. Bauer, *Phys. Rev. Research* **3**, 033188 (2021).
- [43] P. Coleman, *Introduction to many-body physics* (Cambridge University Press, 2015).
- [44] C. Wagner, T. Chowdhury, J. H. Pixley, and K. Ingersent, *Phys. Rev. Lett.* **121**, 147602 (2018).
- [45] E. S. Sørensen, M.-S. Chang, N. Laflorencie, and I. Affleck, *J. Stat. Mech.: Theory Exp.* **2007**, L01001 (2007).
- [46] E. S. Sørensen, M.-S. Chang, N. Laflorencie, and I. Affleck, *J. Stat. Mech.: Theory Exp.* **2007**, P08003 (2007).
- [47] I. Affleck, N. Laflorencie, and E. S. Sørensen, *J. Phys. A: Math Theor.* **42**, 504009 (2009).
- [48] E. S. Sørensen and I. Affleck, *Phys. Rev. B* **53**, 9153 (1996).
- [49] L. Borda, *Phys. Rev. B* **75**, 041307 (2007).
- [50] A. Holzner, I. P. McCulloch, U. Schollwöck, J. von Delft, and F. Heidrich-Meisner, *Phys. Rev. B* **80**, 205114 (2009).
- [51] V. Barzykin and I. Affleck, *Phys. Rev. B* **57**, 432 (1998).
- [52] J. Haegeman, J. I. Cirac, T. J. Osborne, I. Pižorn, H. Verschelde, and F. Verstraete, *Phys. Rev. Lett.* **107**, 070601 (2011).
- [53] J. Haegeman, C. Lubich, I. Oseledets, B. Vandereycken, and F. Verstraete, *Phys. Rev. B* **94**, 165116 (2016).
- [54] I. H. Kim and B. Swingle, [arXiv:1711.07500](https://arxiv.org/abs/1711.07500) (2017).
- [55] T. J. Sewell, C. D. White, and B. Swingle, [arXiv:2210.16419](https://arxiv.org/abs/2210.16419) (2022).
- [56] As a technical but important detail, in order to completely diagonalize the correlation matrix for a finite-sized system, the right boundary of the chain is treated by the GMPS procedure, which creates large non-zero mutual information at the tail as well as some finite values at limited intermediate sites.
- [57] K. Okunishi and T. Nishino, *Phys. Rev. B* **82**, 144409 (2010).
- [58] Since we focus on the interaction at the impurity site 1 and the impurity mutual information (first row of the matrix) contains all necessary entanglement information, emergent models are taken from the impurity mutual information  $I(1, r)$  with cutoffs, for both ground state energies and dynamics.
- [59] A. Georges, G. Kotliar, W. Krauth, and M. J. Rozenberg, *Rev. Mod. Phys.* **68**, 13 (1996).
- [60] Note that the mutual information  $I(1, r) = 0$  for all  $r$  immediately after the quench, but then becomes quickly



stabilized with fixed peak locations except at certain isolated times.

- [61] However, they are relevant when determining particle numbers in coarse-grained models. Given the total particle  $N - 1$  ( $-1$  for impurity annihilation), inactive sites give close to 0 or 1 diagonal matrix elements in the diagonalized correlation matrix, whose summation  $N_{\mathcal{I}}$  gives the corresponding particle number in the coarse-grained model by  $N_{\mathcal{A}} = N - N_{\mathcal{I}} - 1$ .
- [62] <https://github.com/ITensor/ITensors.jl/tree/main/ITensorGaussianMPS>.
- [63] M. Fishman, S. R. White, and E. M. Stoudenmire, *SciPost Phys. Codebases*, 4 (2022).
- [64] J. Bezanson, A. Edelman, S. Karpinski, and V. B. Shah, *SIAM Rev.* **59**, 65 (2017).
- [65] D. Rogerson, F. Pollmann, and A. Roy, *J. High Energy Phys.* **2022**, 165 (2022).